Ultra-Wideband Frequency Modulated Continuous Wave Photonic Radar System for Three-Dimensional Terahertz Synthetic Aperture Radar Imaging

Li Yi, *Member, IEEE*, Ryohei Kaname, Ryoko Mizuno, Yihan Li, *Member, IEEE*, Masayuki Fujita, *Member, IEEE*, Hiroshi Ito, *Fellow, IEEE*, and Tadao Nagatsuma, *Fellow, IEEE*

***Abstract*—Three-dimensional (3D) imaging remains an expensive and challenging task in the THz band. In this study, a frequency-modulated continuous-wave photonic radar system was presented in the 300-GHz band, instead of using electronic-based devices. The proposed system can obtain a 6-dB bandwidth of 120 GHz to achieve a range resolution of ∼1.1 mm. The frequency sweep linearity of a laser source was calibrated with respect to the imaging distance and range resolution, through which a maximum detectable distance of ∼800 mm was achieved with the collimated beam. To obtain the desired 3D information, the synthetic aperture radar (SAR) technique was introduced to the proposed system to achieve 3D imaging, which was not bounded by the fixed focal distance of a focus lens. It can provide a spatial resolution of ∼1.5 mm within a 3D imaging range up to ∼300 mm. The potential and limitations of SAR imaging schemes are discussed based on the theoretical and experimental results.**

***Index Terms*—Frequency-modulated continuous-wave radar, photomixing, photonic radar, synthetic aperture radar, terahertz imaging.**

I. Introduction

In RECENT years, terahertz (THz) imaging techniques have been widely studied for inspection applications owing to their sub-millimeter-level resolution and transparency. A precise THz image is crucial for a variety of applications ranging from non-destructive testing and security to medicine, food inspection, and agriculture [1]–[5]. Although many THz imaging systems exhibit excellent performance for two-dimensional (2D) imaging applications [6]–[10], rich three-dimensional (3D) information, such as layers, cavities, and adhesive joints, remains impractical to obtain in the THz band owing to hardware limitations, such as low output power, slow data acquisition, high cost, and limited imaging distance. In conjunction with the rapid development of THz devices, the improvement of 3D THz imaging techniques is urgently required.

The fixed depth of focus (DOF) of a quasi-optic lens is a bottleneck for imaging targets at different distances within a 3D space. Instead of using a focus lens to obtain a spatial resolution, the synthetic aperture radar (SAR) imaging technique is typically applied in the microwave domain [11], [12]. Moreover, it refers to the migration technique in seismic exploration and ultrasonic imaging [11], [13]. The reflected pulse response obtained at different observation distances and angles from different imaging targets can be processed with algorithms to obtain both range and spatial resolution in a 3D space [12]. Such advantages have attracted considerable attention from researchers in the fields of THz [14]–[18]. Owing to the aforementioned hardware limitations, many studies have primarily focused on using a vector network analyzer (VNA) and millimeter-wave (MMW) multiplier to generate THz continuous wave (CW) signals. Further, the pulse signal can be synthesized using the stepped-frequency continuous-wave (SFCW) technique for the enhanced power and signal-to-noise ratio compared with direct pulse generation [19]. Such electronic-based devices can provide excellent output power and a 3D imaging range of ∼2 m was demonstrated with a spatial resolution of ∼2 mm in the 200-GHz band [16]. However, the difficulty in achieving wider bandwidth and higher frequencies with electronic-based devices has increased and their extreme costs make them poorly suited for practical applications [18].

As suggested in several previous studies, phonics-based devices have remarkable potential at higher frequencies of the THz band [20]–[23]. The down-converted optic signal permits an ultra-wide bandwidth, fast frequency sweep, and reduced phase noise. Although THz pulse signal can be directly obtained with photonics-based devices, the synthesized pulse obtained with CW radar and/or swept-source optical coherence tomography (SS-OCT) techniques can provide higher power with a simpler system [1], [8], [23]. Owing to the fast frequency sweep speed in the optic domain, the frequency-modulated continuous-wave

Manuscript received 25 February 2022; revised 27 May 2022 and 12 July 2022; accepted 13 July 2022. Date of publication 25 July 2022; date of current version 21 October 2022. This work was supported by the Japan Society for JSPS Grants-in-Aid for Scientific Research Grant-in-Aid for Early-Career Scientists under Grant 19K14995, ROHM Co., Ltd. and in part by the Core Research for Evolutional Science and Technology (CREST) Program of Japan Science and Technology Agency under Grant JPMJCR21C4. *(Corresponding author: Li Yi.)*

Li Yi, Ryohei Kaname, Ryoko Mizuno, Masayuki Fujita, and Tadao Nagatsuma are with the Graduate School of Engineering Science, Osaka University, Toyonaka, Osaka 560-8531, Japan (e-mail: yi@ee.es.osaka-u.ac.jp; kaname.ryohei@mail.canon; u955300c@ecs.osaka-u.ac.jp; fujita@ee.es.osaka-u.ac.jp; nagatuma@ee.es.osaka-u.ac.jp).

Yihan Li is with the School of Electronics and Information Engineering, Beihang University, Beijing 100191, China (e-mail: yihanli@buaa.edu.cn).

Hiroshi Ito is with the Center for Natural Sciences, Kitasato University, Sagamihara, Kanagawa 252-0373, Japan (e-mail: h.ito@kitasato-u.ac.jp).

Color versions of one or more figures in this article are available at https://doi.org/10.1109/JLT.2022.3193397.

Digital Object Identifier 10.1109/JLT.2022.3193397

(FMCW) technique is considered a promising method for fast 3D imaging systems in the THz band [24]–[28]. As reported in [26], a THz imaging system using a photoconductive antenna (PCA) can provide tunable frequencies ranging from 0.1 THz to a few THz with ∼15 ms, which can be used to measure thicknesses of a few micrometers. However, it has a limited imaging range owing to the low output power and sensitivity of PCA and focus lenses. In comparison, a uni-traveling-carrier photodiode (UTC-PD) is another candidate for photonics-based imaging systems, which can provide a higher output power of microwatt-order in MMW/THz bands [29]. In previous studies, a 600-GHz band SS-OCT system enabled with UTC-PD was proposed with a range resolution of ∼0.61 mm [23]. However, the 3D imaging range was also limited by the focus lens and the data acquisition time was ∼2 s owing to the homodyne detection scheme of SS-OCT. Recently, we upgraded the previous system with the FMCW technique for a reduced data acquisition time of ∼30 ms [25]. The system exhibited a detectable distance of ∼600 mm with a collimated beam. Based on these results, the SAR technique is expected to be introduced to achieve both high-resolution and long-range 3D imaging.

This study demonstrates a photonics-based FMCW system that operates in the 300-GHz band. Owing to the superior performance of the UTC-PD and a THz detector, that is, the Fermi-level managed barrier diode (FMBD) [30], 3D imaging with the SAR technique was demonstrated with a small output power of ∼15 μW. The potential and limitations of SAR schemes are further discussed herein by comparing and evaluating the SAR and real aperture imaging results obtained with the focus lens.

The remainder of this paper is organized as follows. The photonics-based FMCW system in the 300-GHz band is introduced in Section II. The range resolution and detectable range are experimentally investigated. In addition, the problem of nonlinearity of the laser frequency sweep is addressed, and a calibration method to reduce the nonlinearity is applied to enhance the range resolution and detectable distance. The details of the SAR imaging technique for the THz band are provided in Section III. The resolution issue is mainly discussed with both theoretical and experimental results. Finally, a conclusion is provided, along with a discussion in Section IV.

II. Frequency-Modulated Continuous-Wave (FMCW) Photonic Radar System

A. Experimental Configuration and System Characteristics

The FMCW radar technique has been widely applied to microwave radars, MMW radars, and LiDAR sensors. Its theory has been extensively studied in the microwave radar society [12], [28], as summarized in Fig. 1. When a linear chirp signal T_x transmitted to a reflector with a distance of d, the reflected signal R_x with a time delay $\frac{2d}{c}$ can be generated, where c is the velocity of light. Multiple reflections with different time delays will be separated in the frequency-time domain, as shown in Fig. 1(a).

In order to obtain the time delay information, the intermediate frequency (IF) signal can be obtained by mixing the chirp signal

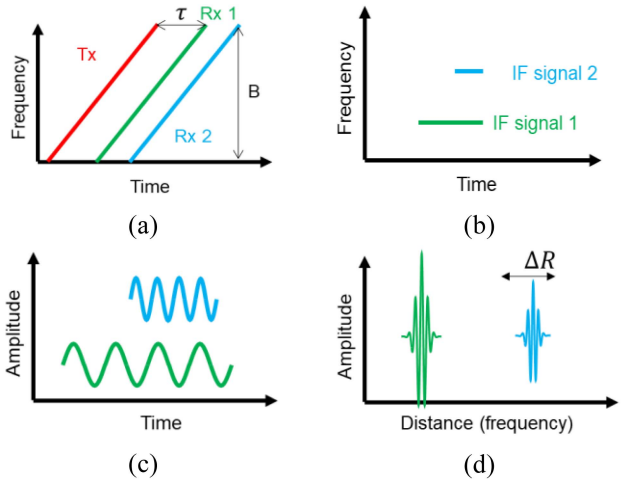

Fig. 1. Concept of the FMCW radar technique: (a) Transmitted chirp signal T_x and two reflected signals R_x in the frequency-time domain; (b) IF signal obtained by mixing T_x and R_x; (c) IF signal in time domain; (d) IF signal after FFT.

T_x and R_x as follows:

$$s(t) = \eta \sin\left(\frac{4\pi d}{c}(v_s t + f_{min}) + \varphi_n(t)\right), \quad (1)$$

where η is the amplitude of IF signal, which is proportional to the reflectivity of the imaging target, f_{min} is the lower frequency of linear chirp, φ_n is the phase noise caused by laser signal, and v_s is the frequency sweeping speed of the chirp signal. As it is indicated in Fig. 1(b) and (c), the frequency component of IF signal is the frequency difference of T_x and R_x, which is proportional to the distance to a imaging target. It is dominant for calculating the range information by applying the fast Fourier transform (FFT) approach, and the targets at different distances correspond to different IF frequencies, as shown in Fig. 1(d). Meanwhile, the phase component of IF signals provides more precise range information, which is vital for doppler-radar applications [28]. Notably, the complex values, phase noise φ_n, and high-frequency components were neglected for imaging applications in this work, and more details can be referred to the Appendix A. This step replaced the homodyne detection of each frequency in SFCW and SS-OCT techniques. The range resolution of the FMCW system can be expressed as follows:

$$\Delta R = \frac{c}{2B}, \quad (2)$$

where ΔR is the range resolution, and B is the bandwidth of the chirp signal. This indicates that the wideband chirp signal and its mixing process are the keys to the FMCW technique to obtaining a high resolution. Although it is already a well-developed technique in the microwave band, wideband chirp signals are difficult to generate and mix at higher frequencies, as mentioned in Section I.

Thus, photonic techniques were adopted to realize the FMCW radar system in the THz band. Fig. 2(a) shows a block diagram of the proposed system and Fig. 2(b) shows a photograph of the experimental setup. A Michelson interferometer was applied using

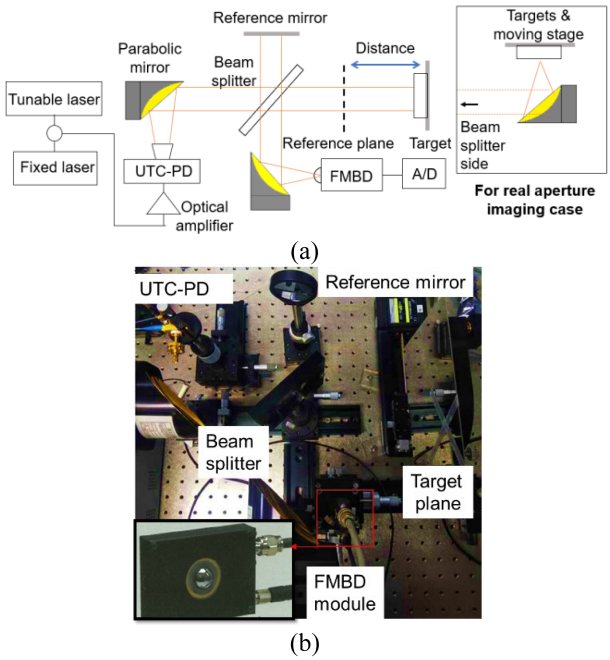

Fig. 2. Experimental setup of the THz FMCW system: (a) Block diagram; (b) Photo of the experimental setup.

a beam splitter instead of a mixer and the photomixing technique was used to generate a fast frequency-swept THz source. To obtain the chirp signal with wide bandwidth, a UTC-PD was applied for its ultra-wide frequency bandwidth and high output power. Notably, the applied UTC-PD was integrated with the metal waveguide of WR-2.8. Although it will limit the bandwidth of UTC-PD, such integration is essential for future system integration with a pre-amplifier to enhance the output power. The frequency of the transmitted THz beam was determined by the frequency difference between the two lasers. To generate the chirp signal, the frequency of one laser was fixed, whereas the frequency of the other laser was swept for a specific frequency range. In the experiment, the wavelength of the fixed wavelength laser was 1550.00 nm and that of the tunable laser was swept from 1546.64 nm to 1548.40 nm. Hence, a chirp signal between 200 and 420 GHz can be generated. The tunable laser operated at a speed of 50 nm/s, which corresponded to a frequency sweeping speed v_s of 6.25 THz/s. The data acquisition time of ∼35 ms with the proposed system, which is the key advantage of using the photonics-based device. The output power from the PD for a typical measurement was approximately 15 μW. The generated THz beam was emitted from a conventional horn antenna of 26 dB gain connected to the UTC-PD and collimated by a parabolic mirror. The collimated beam was divided into two paths using a pellicle beam splitter: one to the reference mirror and the other to the object being tested. Finally, both reflected beams were combined with the beam splitter and received by a quasi-optic lens-integrated FMBD module as a square-low detector with a superiority sensitivity of ∼3 MV/W in the 300-GHz band [30]. In the previous study, such coherent detection scheme was validated for achieving the SS-OCT application [23]; due to a faster frequency sweep speed, the IF signal include the time

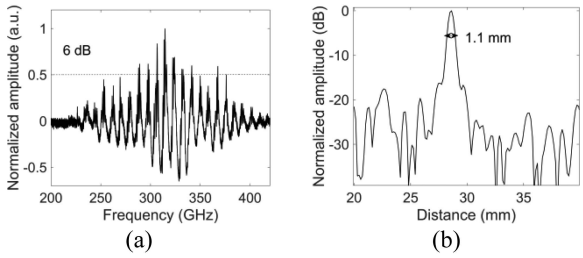

Fig. 3. The characteristics of IF signal from a mirror reflector at a distance of 28 mm: (a) Normalized IF signal in frequency domain; (b) Envelope of time domain signal.

delay information can be obtained with heterodyne detection scheme using (1).

Because of the broad RF frequency bandwidth and high sensitivity of FMBD, mixing of the 220-GHz bandwidth could be achieved. To evaluate the performance of the detected signal with the proposed system, the IF signal of a mirror reflector located at 28 mm away from the reference plane was obtained. The result is shown in Fig. 3(a), the sinusoidal IF signal indicated that the heterodyne scheme with the proposed system was achieved, with a 6-dB bandwidth of ∼120 GHz. The reduced bandwidth at both sides is mainly caused by the integrated metal waveguide of UTC-PD.

Finally, the reflected pulse signal can be obtained after the FFT as it is shown in Fig. 3(b), which indicates a distance of 28 mm. The full width at half-maximum (FWHM) of the reflected signal is ∼1.1 mm, which is larger than the theoretical range resolution expressed in (4). This is caused by the metal waveguide as earlier addressed. Notably, the distance obtained with FFT indicates that the distance between the transmitter and the reference mirror was excluded. For example, the distance between the UTC-PD and the reference mirror was ∼160 mm and the reflector mirror was positioned at a distance of ∼188 mm from the UTC-PD along the propagation path of the THz beam.

B. Calibration on the Nonlinearity of the Frequency Sweep

As introduced in Section II.A, a tunable laser was applied to generate a chirp signal. However, commercial tunable laser devices that use the Littman-Metcalf technique for frequency sweeps cannot preserve perfect linearity within the range of the frequency sweep in the THz domain owing to the mechanical movement of the scanning mirror inside the laser device [31]. For example, the frequency shift at each swept frequency can be obtained as shown in Fig. 4(a) by comparing the acquired IF signal of a reflector mirror at a distance of 28 mm with its theoretical expression using (1). In addition, the random phase noise caused by a slight environmental change reduces the linearity of the laser. Under such conditions, the obtained IF signal can be expressed as:

$$s(t) = \eta \sin\left(\frac{4\pi d}{c}\left(v_s t + f_{min} + F_{err}\sin 2\pi f_m t + \varphi_n(t)\right)\right), \tag{3}$$

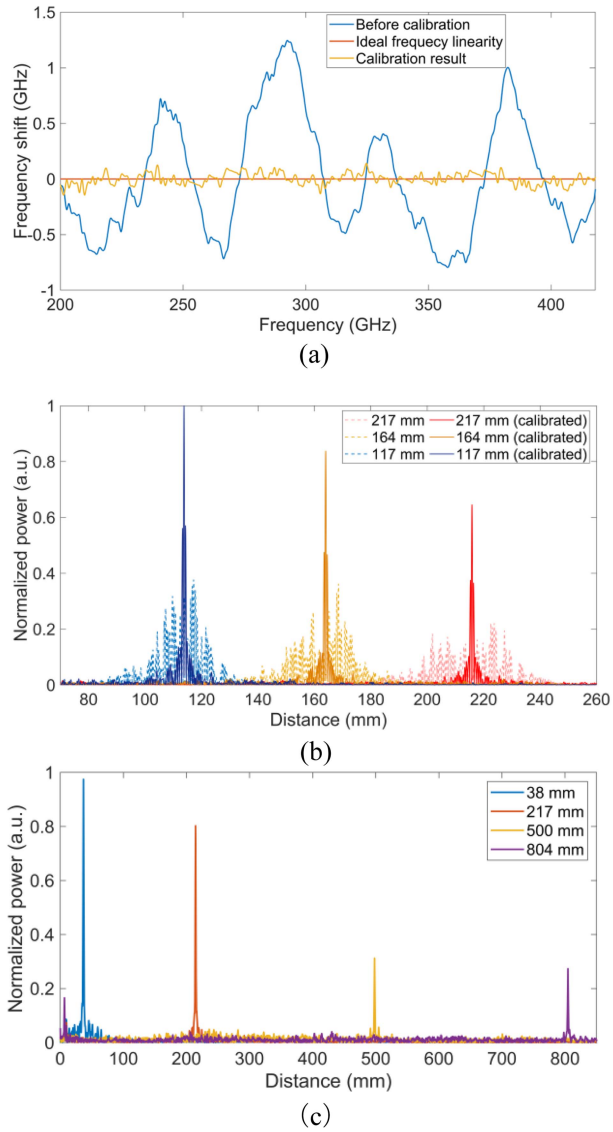

Fig. 4. Calibration on the nonlinearity of the frequency sweep: (a) Frequency shift at each swept frequency; (b) Reflected signals before/after calibration at different distances; (c) Imaging distance of the calibrated signal.

where $F_{err}\sin 2\pi f_m$ denotes the periodic frequency trend shown in Fig. 4(a), f_m is the rotation frequency of the scanning mirror inside the laser device, and φ_n is the phase noise. As indicated in [32], [33], such nonlinear components and random phase noise will cause sidelobes after the FFT; thus, the range resolution and dynamic range will be reduced. In this case, corrections on the nonlinearity of the frequency sweep are required for FMCW systems in practice [33]. A simple calibration method introduced in [25] was applied to the proposed system. The core idea is to use reference data obtained with a reflector mirror fixed at a known distance. The calibration parameters can then be calculated by analyzing the differences between the reference data and the numerical simulation of the IF signal with a known distance. The calibrated results are shown in Fig. 4(b), where the reflected signals at longer imaging distances are significantly improved. However, such simple calibration can mainly correct the nonlinearity caused by $F_{err}\sin 2\pi f_m$, whereas the phase noise cannot be fully corrected. As shown in Fig. 4(a), a slight frequency shift still exists after the calibration, causing weak sidelobes, as shown in Fig. 4(b).

Furthermore, the applied laser sweeping speed of 50 nm/s does not correspond to its maximum speed. However, the linearity worsens for higher sweeping speeds for this equipment; therefore, a higher sweeping speed was not used. In addition, a dwell time of ∼200 ms between consecutive wavelength sweeping is required for the laser employed in the experiment to reset, which limited the imaging speed of the current system. A more stable laser source with higher linearity and a faster sweeping speed is the key for photonic radar imaging at a longer imaging distance. For example, chirp signal generation based on the principle of precisely reoccurring frequency shifting is proposed to generate an MMW frequency-modulated signal of up to a 40-GHz bandwidth with substantially improved linearity [34]. The photonic sources specified for THz photonic radar applications are expected to be developed in the future.

As demonstrated above, the reflected signals from longer distances were severely distorted by the nonlinearity of the laser device. However, these reflections can be partially recovered by calibration processing. Here, the changes in reflection when the distance of the reflector mirror was increased are shown in Fig. 4(c). Owing to the limited experimental space, the reflected signal up to 800 mm was detected with a 300-GHz band system with small output power. However, such imaging distances were achieved with careful calibration and specified for a single target. Generally, when the target is not an ideal reflector but includes multiple reflections, an imaging distance of ∼500 mm could be achieved in practice. Besides, the periodic frequency trend shown in Fig. 4(a) was stable within a data acquisition campaign of a few hours, but another calibration was usually required after a few days.

Although the collimated beam cannot be directly applied for imaging applications because of the lack of spatial resolution, it is suitable for thickness measurements where high spatial resolution is not required. For example, we applied a collimated beam to inspect the thickness changes of the coating material with a thickness of ∼500 μm. A slight thickness change of ∼50 μm can be monitored with the proposed system in the 600-GHz band and it shows adequate agreement with the measurement results obtained using the THz pulse system [27]. This system can be applied to inspect coating materials at large scales, such as for ships and planes [35]. Such a long detectable distance with a collimated beam indicates the possibility of introducing the SAR scheme in the THz band to obtain 3D imaging.

III. Synthetic Aperture Imaging in the THz Band

A. Real and Synthetic Aperture Imaging

To obtain the imaging results from the radiated THz beam, a real aperture system with quasi-optic components or the SAR imaging technique is necessary, as shown in Fig. 5. The real aperture imaging system, which consists of quasi-optic lenses, is widely applied in many existing THz imaging systems [6]–[9]. Real aperture imaging can be achieved using an extra parabolic

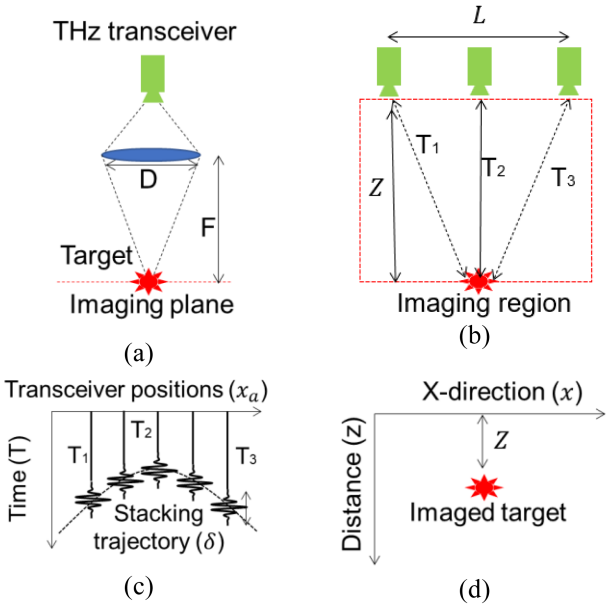

Fig. 5. Concept of real and synthetic aperture imaging configuration: (a) Real aperture imaging using a focus lens; (b) SAR imaging configuration; (c) Corresponding radar profile of a single target as shown in (b); (d) Ground truth/SAR imaging result.

mirror based on the proposed system, as shown in Fig. 2. The spatial resolution obtained with a focus lens is limited by the diffraction limit, which can be expressed as follows:

$$\Delta x \approx 0.61 \frac{\lambda F}{D}, \tag{4}$$

where Δx indicates the spatial resolution, λ is the wavelength, F is the focal length, and D is the aperture of the lens. Owing to the narrow THz beam from the horn antenna, the effective beam width was much smaller than the mirror aperture, which resulted in a reduced spatial resolution compared to that calculated using (4). This also occurs in many quasi-optic-based THz imaging systems [6], [7], [9]. Practically, a spatial resolution of ~1 mm can be obtained in the 300-GHz band. However, owing to the fixed focal length as shown in Fig. 5(a), real aperture imaging is not suitable for 3D imaging when the imaging planes are distant from the focus point. Although advanced lens design techniques can improve the DOF to increase the 3D imaging range, real 3D imaging is difficult to be achieved with a fixed focal distance [36].

In contrast, SAR image processing was widely used for medical imaging, seismic exploration, and microwave imaging [12], [13]. It has many variations depending on the imaging targets and the data domain. For example, microwave air-born radars focus on far-field targets and are usually applied in the frequency domain, where the range and the spatial resolution are considered to be independent [12]; however, the back projection or diffraction stacking migration for ultrasonic imaging mainly operates in the time domain [13]. This method considers the spherical wavefront in the Fresnel region, where the range and spatial resolution are related as follows:

$$\Delta x \approx \frac{cZ}{4BL}, \tag{5}$$

where Z is the distance between the target plane and THz transceiver, as shown in Fig. 5(b), and L is the aperture length of the moving THz transceiver or array sensors. Notably, the radiation pattern of the THz antenna determines the effective aperture; hence, the spatial resolution is also influenced. As suggested in (4) and (5), the SAR imaging approach is more suitable for 3D imaging since it can provide a stable imaging resolution at different imaging distances [11], [13], [37]. Practically, the spatial resolution of the SAR imaging system needs to be evaluated using experimental results, which are introduced in Section III.B.

The time-domain SAR algorithm was applied because it can intuitively observe the imaging procedure [11], [13]. Depending on the observation of a radar profile, as shown in Fig. 5(c), a proper imaging area can be selected to reduce the calculation cost for 3D imaging by considering the effective aperture and target position. Besides, the physical meaning of time domain SAR algorithm is straightforward, as shown in Fig. 5(b), (c), and (d). Every imaging point is assumed to be a potential target, and by calculating the hyperbolic travel time in the data domain, we can sum all the amplitudes along this trajectory onto the imaging point. When the imaging point coincides with an existing scatter target, the summing energy can be enhanced to image the target. The 2D diffraction stacking algorithm can be expressed as follows:

$$m(x,z) = \iint d(t,x_a) \cdot \delta(t - T) \cdot e^{2\pi f_{min} T} dt dx_a, \tag{6}$$

$$T = \frac{2\sqrt{z^2 + (x - x_a)^2}}{c}, \tag{7}$$

where x and z are the imaging points, x_a is the position of the THz transceiver, and T is the two-way travel time between the THz transceiver and the target. Notably, phase compensation is required with $e^{2\pi f_{min} T}$ to ensure the coherency of IF signals at different traces. Although the sampling interval between THz transceivers is still limited by the Nyquist criterion with conventional methods expressed in (6), the sparse array theory can reduce the sampling data or sensor number of a THz array [37], [38].

B. Synthetic Aperture Imaging Experiments

The configuration of the proposed photonic radar system for SAR imaging is shown in Fig. 6, which is considerably simplified compared to real aperture imaging system shown in Fig. 2. The same UTC-PD with an output power of ~15 μW and FMBD were used as that of the 300-GHz system introduced in Section II.A. The operating frequency ranged from 200 to 420 GHz, which provided a range resolution of ~1.1 mm, as shown in Fig. 3(b). Although the beam collimation is not required, the reflected signal from the targets and reference mirror combined with a beam splitter and the FMBD operates as a mixer to generate the IF signal. The transmitter and receiver are

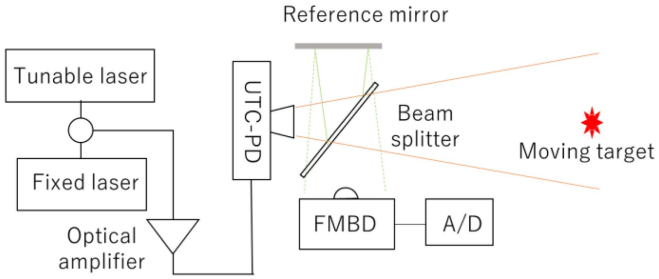

Fig. 6. Experimental configuration for SAR imaging.

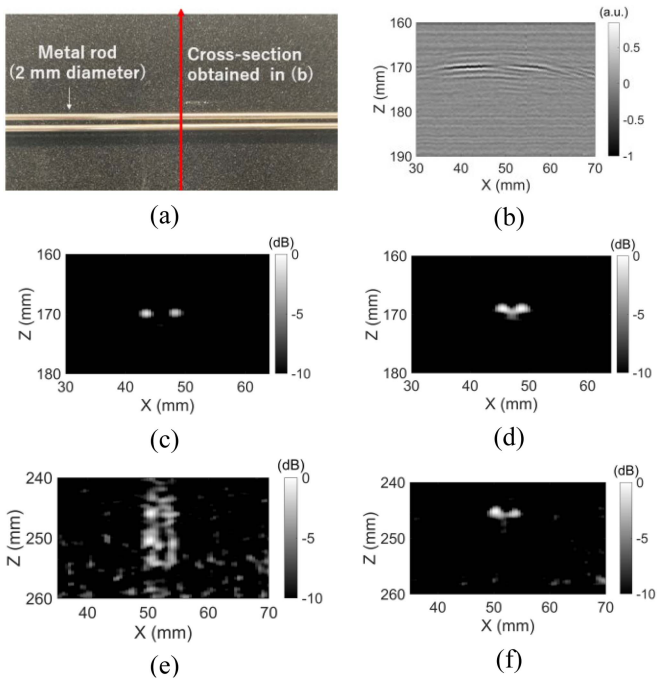

Fig. 7. SAR imaging results of a pair of metal rods: (a) Configuration of the metal rods target; (b) Radar data of the metal rods at a distance of ∼170 mm with a gap of 3 mm in between; (c) SAR imaging result for the configuration of (b); (d) SAR imaging result with a reduced gap of 1.5 mm; (e) SAR imaging result with an increased distance of ∼250 mm without linearity calibration; (f) SAR imaging result with an increased distance of ∼250 mm.

installed at the same distance of 30 mm from the beam splitter for obtaining the coherency of reference and reflected signal, and such a zero-offset configuration is known as a monostatic system for the SAR system.

Two metal rods with a diameter of 2 mm and separated by a small gap of 3 mm were fixed as the imaging target, as shown in Fig. 7(a). Furthermore, the cross-section data with a 100-mm aperture length were obtained by sampling across the two rods with a spatial sampling interval of 0.5 mm. The imaging distance to the metal rods was ∼170 mm. The radar profiles after linearity calibration and FFT are shown in Fig. 7(b). Data were processed with conventional time-domain SAR processing introduced in Section III.C, and the imaging result is shown in Fig. 7(c). The hyperbolic curvature indicates that such imaging conditions are not perfect for far-field assumptions and time-domain processing is more suitable than the conventional air-born SAR

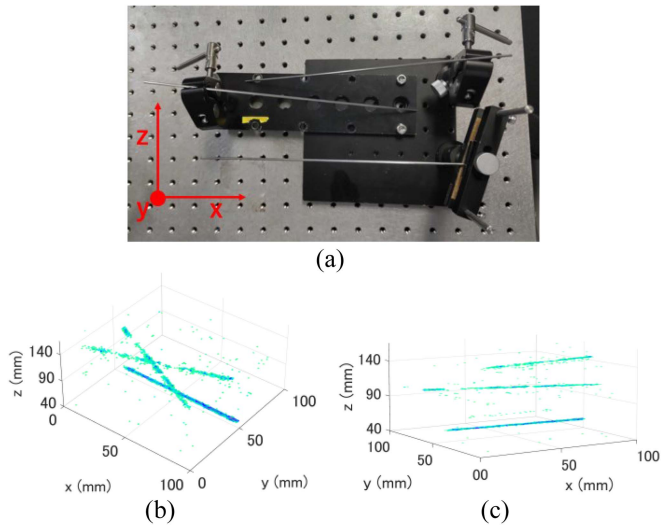

Fig. 8. SAR imaging result of the 3D distributed rods: (a) Imaging model; (b) Top view of the 3D imaging result; (c) Side view of the 3D imaging result.

processing [13]. The minimum distance of 1.5 mm between the two rods can be separated at the same imaging distance as that of Fig. 7(d). The spatial resolution was slightly reduced compared to real aperture imaging. This reduction is caused by the bandwidth and effective aperture of SAR processing, as indicated in (7). Although the effective aperture of the transceiver pair is difficult to analyze owing to the differences in the horn antenna and lens installed with FMBD, it can be observed from Fig. 7(b) that the effective aperture is ∼30 mm, which is much smaller than the full aperture length of 100 mm. The targets were also evaluated at different imaging distances; the 1.5-mm gap can be recognized at a maximum distance of ∼250 mm, as shown in Fig. 7(e) and (f). The reduction in the imaging distance is caused by the un-collimated beam and the calibration process, which is explained in Section II.B.

To present the 3D imaging ability of the proposed system, three metal rods with a diameter of 2 mm are distributed at different angles within a range of 100 mm, as shown in Fig. 8(a). The imaging distances of the three rods are ∼50 mm, ∼110 mm, and ∼150 mm. The model was mounted on a two-axis moving stage to obtain a 2D scanning region of 100 mm × 100 mm, with a spatial interval of 0.5 mm. Approximately 1 h was required for data acquisition, limited by the acquisition speed bottleneck described in Section II.B. The 3D imaging results at different angles are shown in Fig. 8(b) and (c). As observed, the spatial resolution did not reduce with the increasing imaging distance and all the rods were imaged clearly, as described in Section III.B. However, owing to the increasing imaging distance, the rods at longer distances become weak owing to the un-collimated beam.

Finally, the 3D imaging results were evaluated and compared with the real aperture imaging results using a simple layer model, as shown in Fig. 9. A blade and a coin were fixed between each layer of 2-mm-thick acrylic plates. Real aperture imaging can be obtained by introducing an extra parabolic mirror, as shown in Fig. 2(a). As introduced in Section III.A, a trade-off exists between the spatial resolution and the DOF for the 3D imaging

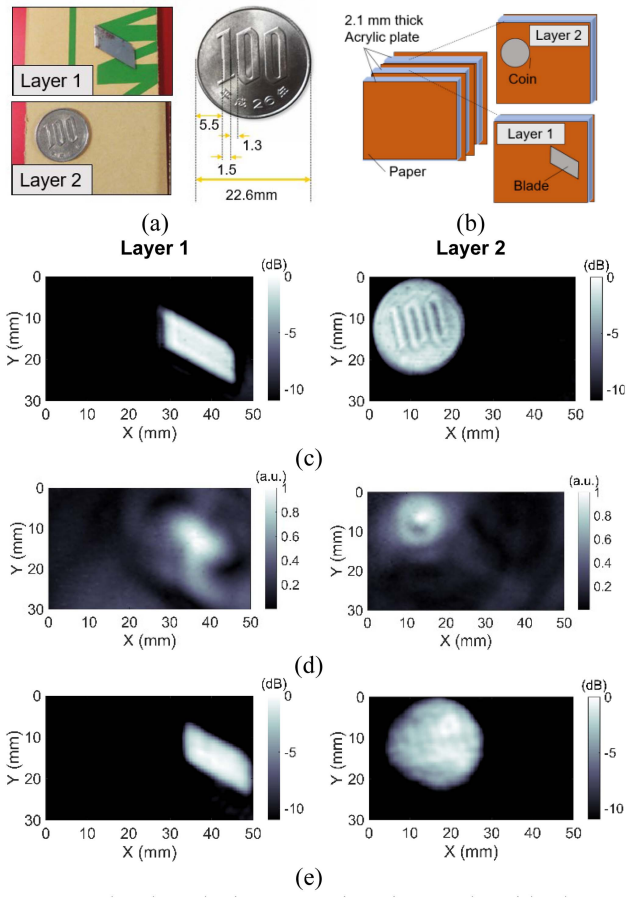

Fig. 9. Real and synthetic aperture imaging results with a layer model: (a) Targets inside the layer model; (b) 3D structure of the layer model; (c) Real aperture imaging results at imaging planes with a blade and a coin; (d) Raw data obtained at imaging planes with a blade and a coin using the SAR scheme; (e) SAR imaging results at imaging planes with a blade and a coin.

case [36]. Here, a hyperbolic mirror with a focal length of 5 cm, mirror aperture of 15 cm, and DOF of ∼1 cm was installed to cover the 3D imaging region within a thickness of ∼1 cm. To obtain clear imaging results, the 30 mm × 50 mm imaging was sampled with spatial intervals of 0.25 mm. The layers including the blade and the coin are shown in Fig. 9(c), where numbers "1" and "0" printed on the coin could be distinguished with a spatial resolution of ∼1 mm.

In contrast, the imaging distance for the SAR scheme is 150 mm to obtain a larger effective aperture. Data were obtained with a spatial interval of 0.5 mm, which is larger than that of the real aperture imaging case. The spatial resolution of SAR imaging does not rely on dense spatial sampling; therefore, the sparse sampling scheme can be a key advantage of using the SAR imaging scheme [37], [38]. The raw data shown in Fig. 9(d) indicates an effective aperture of ∼30 mm, where the shapes of both targets are entirely blurred. The imaging results after SAR processing are shown in Fig. 9(e). Consequently, both targets were restored to their original shapes. However, the letters on the coin are less clear than those obtained with the real aperture system, owing to the weak reflections and reduced spatial resolution. As earlier addressed, the limited effective aperture can be the main reason for the reduced spatial resolution. A specific antenna design with a wider beamwidth is required for SAR imaging instead of a conventional horn antenna. In addition, the numerical calculations and imaging algorithms can change the spatial resolution; more complicated algorithms, such as compressed sensing and deconvolution techniques can be introduced to THz imaging to enhance the spatial resolution [37]–[40].

IV. Conclusion and Discussion

A THz FMCW system enabled with photonics techniques is proposed for the 300-GHz band. The maximum detectable distance of up to 800 mm with a range resolution of ∼1.1 mm was achieved with a collimated THz beam. Moreover, the possibility of realizing the photonics-based SAR imaging scheme with a photonics-based system in THz bands was highlighted.

The combination of UTC-PD and FMBD enabled the long imaging distance with a small output power of ∼15 μW and was the key to achieving SAR imaging. Notably, numerical calibration was required for the targets at an imaging distance longer than ∼400 mm owing to the frequency sweep nonlinearity of the tunable laser. However, because the nonlinearity cannot be ideally removed, only the simple imaging targets can be detected at the maximum imaging distance. Hence, a specific sweeping laser source with enhanced frequency sweep linearity is urgently required. Some photonics-based MMW generation techniques can be extended to the THz band to enhance both the frequency sweep speed and linearity [21], [34].

As demonstrated in Section III.B, the SAR technique can be used to realize 3D imaging. Although the SAR imaging results provided a reduced spatial resolution of ∼1.5 mm owing to the resolution dependency on the bandwidth and the insufficient aperture length, the high spatial resolution can be simultaneously obtained at different imaging distances. To further improve the resolution, an accurate design of the THz antenna and/or observation schemes was required for SAR imaging. In addition, numerical algorithms could also enhance the spatial resolution, as reported in [39]–[41]. Furthermore, the sparse array concept with a multistatic scheme would be an alternative approach to phased array systems to realize the real-time THz array 3D imaging system, where complicated phase modulation is not required and the number of THz sensor elements can be reduced [38]. In conjunction with the rapid development of THz hardware, the proposed system shows remarkable potential for next-generation remote sensing applications in the THz band, including high-resolution imaging, monitoring, and classification [42].

Appendix A
Phase Noise in IF Signal and Imaging Result

In this section, the phase noise neglected in (1) will be further discussed. It is clarified that the phase information is coherently obtained by self-mixing the transmitted and received THz chirp signal, while a phase noise component remains with sufficient coherent length. Its effect on ranging and imaging applications is also discussed quantitatively.

As introduced in Section II.A, the transmitted THz chirp signal T_x is generated with the photomixing technique, which can be expressed with:

$$T_x(t) = A_t \sin\left(2\pi t\left(f_{min} + \frac{v_s t}{2}\right) + \varphi_i + \varphi_n(t)\right), \quad (8)$$

where A_t is the amplitude of the transmitted signal, f_{min} is the lower frequency of linear chirp, and v_s is the frequency sweeping speed of the tunable laser. The initial phase of the THz chirp signal is φ_i, which is the phase difference of two laser signal. Notably, it is challenging to lock the phases of a laser precisely, especially for the tunable laser. In this case, a phase noise component φ_n is included with the THz chirp signal.

When the transmitted THz linear chirp signal T_x propagate to a reflector at a distance *d,* the reflected signal R_x with a delay time τ can be expressed as follows:

$$R_x(t) = A_t A_r \sin\left(2\pi(t-\tau)\left(f_{min} + \frac{v_s(t-\tau)}{2}\right) + \varphi_i + \varphi_n(t)\right), \quad (9)$$

where

$$\tau = \frac{2d}{c}, \quad (10)$$

A_r is the amplitude of the received signal. Since the imaging targets in this work are located within a few meters, which is smaller than the coherence length of laser signal, the coherent IF signal s can be obtained by mixing the chirp signal T_x and $R_x$with a square-law detector as follows:

$$s(t) = \frac{A_t A_r}{2} \sin\left(\frac{4\pi d}{c}(v_s t + f_{min}) + \varphi_n(t)\right), \quad (11)$$

which is equivalent to (1) by replacing $\frac{A_t A_r}{2}$ to η, which is proportional to A_t and A_r. The high frequency component of THz signal is neglected by using a low-pass filter, and the initial phase of THz chirp signal φ_i will be canceled during the mixing calculation. Notably, the frequency component of IF signal $\frac{4\pi d}{c} v_s$ is mainly used to calculate the distances between the antenna and targets with FFT; while the phase component of IF signal $\frac{4\pi d}{c} f_{min}$ is also target-dependent but less accurate due to the phase noise φ_n. Although the phase noise is propagated from the optic signal to the THz carrier signal, and then to the low frequency IF signal, it is mostly generated within a short period of τ, which is nanosecond-order for the targets within a few meters. Although the quantitative evaluation of the coherence length with the tunable laser is not included, it can be observed from Fig. 7(b) that the phase of the reflected pulses from the metal rods is continuous, which indicates that the IF signals are coherently obtained. However, some of the discontinuities can also be observed in Fig. 7(b), indicating that a small amount of the phase noise still exists and may reduce the dynamic range of the reflected signal [43]. Since the phase information is also target-dependent, the influence of the phase noise is not critical for imaging applications with complicated targets such as GPR and near-range MMW imaging [19], [39]. The polluted IF signal with phase noise usually results in reduced imaging resolution and imaging artifacts [44]. Meanwhile, phase information becomes essential for advanced radar techniques such as polarization analysis. In this case, observations with different polarization properties and phase calibration are required [45]. In the future, phase calibration will also be introduced to the proposed system to enhance the imaging resolution and/or to obtain doppler information [28], [44].

REFERENCES

[1] D. M. Mittleman, "Twenty years of terahertz imaging," *Opt. Exp.*, vol. 26, no. 8, pp. 9417–9431, 2018, doi: 10.1364/oe.26.009417.

[2] C. Wang, J. Y. Qin, W. D. Xu, M. Chen, L. J. Xie, and Y. B. Ying, "Terahertz imaging applications in agriculture and food engineering: A review," *Trans. ASABE*, vol. 61, no. 2, pp. 411–424, 2018, doi: 10.13031/trans.12201.

[3] P. Hillger, J. Grzyb, R. Jain, and U. R. Pfeiffer, "Terahertz imaging and sensing applications with silicon-based technologies," *IEEE Trans. Terahertz Sci. Technol.*, vol. 9, no. 1, pp. 1–19, Jan. 2019, doi: 10.1109/TTHZ.2018.2884852.

[4] C. Jansen et al., "Terahertz imaging: Applications and perspectives," *Appl. Opt.*, vol. 49, no. 19, pp. E48–E57, 2010, doi: 10.1364/AO.49.000E48.

[5] D. Nüßler and J. Jonuscheit, "Terahertz based non-destructive testing (NDT)," *tm-Technisches Messen*, vol. 88, no. 4, pp. 199–210, 2021, doi: 10.1515/teme-2019-0100.

[6] M. Kim, E. S. Lee, D. W. Park, I. M. Lee, and K. H. Park, "Hexagonal polygon mirror based terahertz imaging system by using telecentric f-Θ lens," in *Proc. Int. Conf. Infrared, Millimeter, Terahertz Waves, IRMMW-THz*, 2019, pp. 1–2, doi: 10.1109/IRMMW-THz.2019.8873863.

[7] R. Kaname, T. Sagisaka, L. Yi, and T. Nagatsuma, "600-GHz-band terahertz imaging system using frequency-independent concave mirror," in *Proc. Int. Topical Meeting Microw. Photon.*, 2020, pp. 58–61, doi: 10.23919/MWP48676.2020.9314504.

[8] L. Yi et al., "Towards practical terahertz imaging system with compact continuous wave transceiver," *J. Lightw. Technol.*, vol. 39, no. 24, pp. 7850–7861, Dec. 2021, doi: 10.1109/JLT.2021.3092779.

[9] K. B. Cooper et al., "Fast high-resolution terahertz radar imaging at 25 meters," *Terahertz Phys., Devices, Syst. IV: Adv. Appl. Ind. Defence*, vol. 7671, pp. 250–257, 2010, doi: 10.1117/12.850395.

[10] H. I. G. Uerboukha and K. A. N. Allappan, "Toward real-time terahertz imaging," *Adv. Opt. Photon.*, vol. 10, no. 4, pp. 843–938, 2018.

[11] C. Özdemir, Ş. Demirci, E. Yiğit, and B. Yilmaz, "A review on migration methods in b-scan ground penetrating radar imaging," *Math. Problem Eng.*, vol. 2014, pp. 1–16, 2014, doi: 10.1155/2014/280738.

[12] D. Oloumi, "Ultra-wideband synthetic aperture radar imaging: Theory and applications," M.S. thesis, Dept. Electr. Comput. Eng., Univ. Alberta, Edmonton, AB, Canada, Sep. 2016.

[13] C. Cafforio, C. Prati, and F. Rocca, "SAR data focusing using seismic migration techniques," *IEEE Trans. Aerosp. Electron. Syst.*, vol. 27, no. 2, pp. 194–207, Mar. 1991, doi: 10.1109/7.78293.

[14] Z. Ou, J. Wu, H. Geng, X. Deng, and X. Zheng, "Confocal terahertz SAR imaging of hidden objects through rough-surface scattering," *Opt. Exp.*, vol. 28, no. 8, pp. 12405–12415, 2020, doi: 10.1364/oe.388392.

[15] Z. Li et al., "Terahertz synthetic aperture in-line holography with intensity correction and sparsity autofocusing reconstruction," *Photon. Res.*, vol. 7, no. 12, pp. 1391–1399, 2019, doi: 10.1364/prj.7.001391.

[16] D. Damyanov, A. Batra, B. Friederich, T. Kaiser, T. Schultze, and J. C. Balzer, "High-resolution long-range THz imaging for tunable continuous-wave systems," *IEEE Access*, vol. 8, pp. 151997–152007, 2020, doi: 10.1109/ACCESS.2020.3017821.

[17] S. Saqueb, N. K. Nahar, and K. Sertel, "Fast two-dimensional THz imaging using rail-based synthetic aperture radar (SAR) processing," *Electron. Lett.*, vol. 56, no. 19, pp. 988–990, 2020, doi: 10.1049/el.2020.0847.

[18] A. Batra et al., "Short-range SAR imaging from GHz to THz waves," *IEEE J. Microw.*, vol. 1, no. 2, pp. 574–585, Apr. 2021, doi: 10.1109/jmw.2021.3063343.

[19] P. K. Verma, A. N. Gaikwad, D. Singh, and M. J. Nigam, "Analysis of clutter reduction techniques for through wall imaging in UWB range," *Prog. Electromagn. Res. B*, vol. 17, pp. 29–48, 2009, doi: 10.2528/PIERB09060903.

[20] T. Nagatsuma et al., "Terahertz wireless communications based on photonics technologies," *Opt. Exp.*, vol. 21, no. 20, pp. 23736–23747, 2013, doi: 10.1364/oe.21.023736.

[21] P. Ghelfi et al., "A fully photonics-based coherent radar system," *Nature*, vol. 507, no. 7492, pp. 341–345, 2014, doi: 10.1038/nature13078.
[22] R. Safian, G. Ghazi, and N. Mohammadian, "Review of photomixing continuous-wave terahertz systems and current application trends in terahertz domain," *Opt. Eng.*, vol. 58, no. 11, 2019, Art. no. 110901, doi: 10.1117/1.oe.58.11.110901.
[23] T. Nagatsuma, T. Ikeo, and H. Nishii, "Terahertz imaging based on optical coherence tomography," *Photon. Res.*, vol. 2, no. 4, pp. B64–B69, 2014, doi: 10.1364/PRJ.2.000B64.
[24] D.-S. Yee, J. S. Yahng, C.-S. Park, H. D. Lee, and C.-S. Kim, "High-speed broadband frequency sweep of continuous-wave terahertz radiation," *Opt. Exp.*, vol. 23, no. 11, pp. 14806–14814, 2015, doi: 10.1364/oe.23.014806.
[25] R. Kaname, L. Yi, and T. Nagatsuma, "Fast three-dimensional terahertz imaging with continuous-wave photomixing," in *Proc. 46th Int. Conf. Infrared, Millimeter Terahertz Waves*, 2021, pp. 1–2, doi: 10.1109/IRMMW-THz50926.2021.9567535.
[26] L. Liebermeister et al., "Optoelectronic frequency-modulated continuous-wave terahertz spectroscopy with 4 THz bandwidth," *Nat. Commun.*, vol. 12, no. 1, Dec. 2021, Art. no. 1071, doi: 10.1038/s41467-021-21260-x.
[27] R. Kaname, L. Yi, and T. Nagatsuma, "Investigation on 600-GHz-band FMCW photonic radar system for a flexible inspection distance," in *Proc. IEEE Asia-Pacific Microw. Conf.*, 2021, pp. 437–439, doi: 10.1109/APMC52720.2021.9661657.
[28] C. Lovescu and S. Rao, *The Fundamentals of Millimeter Wave Sensors*. Dallas, TX, USA: Texas Instruments, May 2017. [Online]. Available: https://www.ti.com/lit/wp/spyy005a/spyy005a.pdf
[29] T. Ishibashi and H. Ito, "Uni-traveling-carrier photodiodes," *J. Appl. Phys.*, vol. 127, no. 3, 2020, Art. no. 031101, doi: 10.1063/1.5128444.
[30] H. Ito and T. Ishibashi, "InP/InGaAs Fermi-level managed barrier diode for broadband and low-noise terahertz-wave detection," *Jpn. J. Appl. Phys.*, vol. 56, no. 1, 2017, Art. no. 014101, doi: 10.7567/JJAP.56.014101.
[31] K. Liu and M. G. Littman, "Novel geometry for single-mode scanning of tunable lasers," *Opt. Lett.*, vol. 6, no. 3, pp. 117–118, 1981, doi: 10.1364/ol.6.000117.
[32] S. A. B. Mansik Jeon, J. Kim, U. Jung, C. Lee, and W. Jung, "Full-range k-domain linearization in spectral-domain optical coherence tomography," *Appl. Opt.*, vol. 50, no. 8, pp. 1158–1163, 2011.
[33] O. Toker and M. Brinkmann, "A novel nonlinearity correction algorithm for FMCW radar systems for optimal range accuracy and improved multi-target detection capability," *Electron.*, vol. 8, no. 11, 2019, Art. no. 1290, doi: 10.3390/electronics8111290.
[34] Y. Lv, Y. Li, C. Yu, L. Yi, T. Nagatsuma, and Z. Zheng, "Photonic generation of highly-linear ultra-wideband stepped-frequency microwave signals with up to $6 \cdot 10^6$ time-bandwidth product," *J. Lightw. Technol.*, vol. 40, no. 4, pp. 1036–1042, 2022, doi: 10.1109/jlt.2021.3127949.
[35] L. Isern, A. J. Waddie, C. Chalk, A. J. Moore, and J. R. Nicholls, "Non-destructive thickness measurement of thermal barrier coatings using terahertz radiation," *Emergent Mater*, vol. 4, no. 6, pp. 1547–1557, 2021, doi: 10.1007/s42247-021-00275-6.
[36] A. I. Hernandez-Serrano and E. Pickwell-MacPherson, "Low cost and long-focal-depth metallic axicon for terahertz frequencies based on parallel-plate-waveguides," *Sci. Rep.*, vol. 11, no. 1, pp. 1–6, 2021, doi: 10.1038/s41598-021-82503-x.
[37] M. E. Yanik and M. Torlak, "Near-field MIMO-SAR millimeter-wave imaging with sparsely sampled aperture data," *IEEE Access*, vol. 7, pp. 31801–31819, 2019, doi: 10.1109/ACCESS.2019.2902859.
[38] X. Zhuge and A. G. Yarovoy, "Study on two-dimensional sparse MIMO UWB arrays for high-resolution near-field imaging," *IEEE Trans. Antennas Propag.*, vol. 60, no. 9, pp. 4173–4182, Sep. 2012, doi: 10.1109/TAP.2012.2207031.
[39] L. Yi, L. Zou, K. Takahashi, and M. Sato, "High-Resolution velocity analysis method using the ℓ-1 norm regularized least-squares method for pavement inspection," *IEEE J. Sel. Topics Appl. Earth Observ. Remote Sens.*, vol. 11, no. 3, pp. 1005–1015, Mar. 2018, doi: 10.1109/JSTARS.2018.2791970.
[40] P. Hillger et al., "A 128-pixel system-on-a-chip for real-time super-resolution terahertz near-field imaging," *IEEE J. Solid-State Circuits*, vol. 53, no. 12, pp. 3599–3612, Dec. 2018, doi: 10.1109/JSSC.2018.2878817.
[41] P. Wang, Z. Li, P. Liu, and Y. Pei, "Super resolution in depth for microwave imaging," *Appl. Phys. Lett.*, vol. 115, no. 4, 2019, Art. no. 044101, doi: 10.1063/1.5098302.
[42] J. Liu, J. Dai, S. L. Chin, and X. C. Zhang, "Broadband terahertz wave remote sensing using coherent manipulation of fluorescence from asymmetrically ionized gases," *Nat. Photon.*, vol. 4, no. 9, pp. 627–631, 2010, doi: 10.1038/nphoton.2010.165.
[43] M. Rezaei and K. Mohammadpour-Aghdam, "On postprocessing reduction of phase noise in FMCW radars," *IEEE Trans. Microw. Theory Techn.*, vol. 68, no. 12, pp. 5103–5114, Dec. 2020, doi: 10.1109/TMTT.2020.3022940.
[44] H. Deng, G. Farquharson, J. Sahr, Y. Goncharenko, and J. Mower, "Phase calibration of an along-track interferometric FMCW SAR," *IEEE Trans. Geosci. Remote Sens.*, vol. 56, no. 8, pp. 4876–4886, Aug. 2018, doi: 10.1109/TGRS.2018.2841837.
[45] D. R. Sheen, A. Freeman, and E. S. Kasischke, "Phase calibration of polarimetric radar images," in *IEEE Trans. Geosci. Remote Sens.*, vol. 27, no. 6, pp. 719–731, Nov. 1989, doi: 10.1109/36.35960.

Li Yi (Member, IEEE) received the B.Sc. degree in geophysics from the School of Ocean and Earth Science, TongJi University, Shanghai, China, in 2011, the M.E. and Ph.D. degrees in environmental studies from the Graduate School of Environmental Studies, Tohoku University, Sendai, Japan, in 2014 and 2017, respectively.

Then, he was a Researcher of the National Institute of Advanced Industrial Science and Technology until 2018. He is currently an Assistant Professor with the Graduate School of Engineering Science, Osaka University, Osaka, Japan. His research interests include photonics-based millimeter/terahertz waves devices and applications, which include sensing/imaging techniques, wireless communication, and signal processing techniques. He is a Member of the Institute of Electronics, Information and Communication Engineers (IEICE), Japan.

Dr. Yi was the recipient of the Student Paper Competition Prize of URSI Japan Radio Science Meeting in 2015, President Award of environmental study of Tohoku University in 2017, and Young Scientists Award of IEICE, SANE, in 2018. He is also an Associate Editor for the *IEICE Electronics Express*.

Ryohei Kaname received the B.E. and M.E. degrees in engineering science from Osaka University, Osaka, Japan, in 2020 and 2022, respectively. In 2022, he joined CANON INC., Tochigi, Japan. His research interests include system development for terahertz imaging and sensing applications.

Ryoko Mizuno received the B.E. degree in engineering science in 2021 from Osaka University, Osaka, Japan, where she is currently working toward the master's degree (second-year), studying under Prof. Tadao Nagatsuma. Her research focuses on terahertz imaging by using resonant tunneling diode transceiver.

Yihan Li (Member, IEEE) received the B.S. degree in physics from the University of Science and Technology of China, Hefei, China, and the Ph.D. degree in electrical engineering from Purdue University, West Lafayette, IN, USA. From 2015 to 2018, he was a Laser Research Scientist with the Boulder Research Lab of IMRA America, Longmont, CO, USA, where he had worked on the development and applications of fiber optical frequency comb. Since 2018, he has been an Associate Professor with the School of Electronics and Information Engineering, Beihang University, Beijing, China. His research interests include microwave photonics, ultrafast optics, optical frequency comb, ultra-wideband signal generation and processing, and photonic THz communications. He is a Member of the Committee of Laser and Terahertz in Space of the Chinese Society of Astronautics and a Member of Optica (the Optical Society of America).

Masayuki Fujita (Member, IEEE) received the Ph.D. degree in ultrasmall and ultralow-threshold microdisk lasers from Yokohama National University, Yokohama, Japan, in 2002.

He joined the Department of Electronic Science and Engineering, Kyoto University, Kyoto, Japan. In 2011, he joined Osaka University, Osaka, Japan, and was appointed the Research Director of the Strategic Basic Research Program CREST, Development of terahertz integrated technology platform through fusion of resonant tunneling diodes and photonic crystals from 2015 to 2021 and has been the Research Director Development of integrated devices and systems to control time domain and space distribution of terahertz waves, since 2021 of the Japan Science and Technology Agency. He is currently an Associate Professor with the Graduate School of Engineering Science, Osaka University. His research interests include photonic crystals, including spontaneous emission control in photonic crystals and high-efficiency light extraction in light-emitting diodes, and silicon light emitters, terahertz materials, devices, systems, and photonic nanostructures, microstructures, and their applications.

Dr. Fujita is a Member of the Japan Society of Applied Physics, Laser Society of Japan, Institute of Electronics, Information and Communication Engineers (IEICE), Japan, Japanese Photochemistry Association, and Optica, formerly OSA. From 1999 to 2002 and from 2003 to 2006, he was a Research Fellow of the Japan Society for the Promotion of Science. He is currently the Vice Chair of the IEICE Technical Committee on Microwave Photonics and Terahertz Photonic-Electronics Technologies, Japan. He was the recipient of various awards, including the IEEE Lasers and Electro-Optics Society Japan Chapter Student Award in 2000, JSAP Young Scientist Presentation Award in 2000, Electronic Material Symposium Award in 2005, JSAP Young Scientist Award in 2006, Research Foundation of Opto-Science and Technology Award in 2007, Paper Award from the LSJ in 2007, and Osaka University Presidential awards for Encouragement during 2013–2015.

Hiroshi Ito (Fellow, IEEE) received the Ph.D. degree in electrical engineering from Hokkaido University, Sapporo, Japan, in 1987.

In 1982, he joined NTT Laboratories, Tokyo, Japan, and was involved in research on MBE and MOCVD growths of III-V materials, and high-speed semiconductor devices including HBTs, FETs, FMBDs, SBDs, UTC-PDs, lasers, and integrated optoelectronic devices. Since 2008, he has been a Professor with Kitasato University, Japan. He was a Visiting Scientist with Stanford University, Stanford, CA, USA from 1991 to 1992, and a Visiting Professor with Hokkaido University from 2011 to 2012. His research interests include ultrafast photonic and electron devices and their applications to terahertz-wave systems.

Prof. Ito is a Senior Member of the Institute of Electronics, Information and Communication Engineers, and a Member of the Japan Society of Applied Physics and the Physical Society of Japan. He was the recipient of the SSDM Paper Award in 2004 and EuMC Microwave Prize in 2006.

Tadao Nagatsuma (Fellow, IEEE) received the B.S., M.S., and Ph.D. degrees in electronic engineering from Kyushu University, Fukuoka, Japan, in 1981, 1983, and 1986, respectively. In 1986, he joined the Electrical Communications Laboratories, Nippon Telegraph and Telephone Corporation (NTT), Atsugi, Japan. From 1999 to 2002, he was a Distinguished Technical Member with NTT Telecommunications Energy Laboratories. From 2003 to 2007, he was a Group Leader with NTT Microsystem Integration Laboratories and was an NTT Research Professor from 2007 to 2009. Since 2007, he has been with Osaka University, Osaka, Japan, where he is currently a Professor with the Division of Advanced Electronics and Optical Science, Department of Systems Innovation, Graduate School of Engineering Science. His research interests include ultrafast electronics and millimeter-wave and terahertz photonics.

Dr. Nagatsuma is a Fellow of the Institute of Electronics, Information and Communication Engineers (IEICE), Japan, and Fellow of the Electromagnetics Academy. He is currently an Associate Editor for the IEEE PHOTONICS TECHNOLOGY LETTERS and the IEEE TRANSACTIONS TERAHERTZ SCIENCE AND TECHNOLOGY, and the President of the Terahertz Systems Consortium and Past-Vice President of the IEICE. He was the recipient of numerous awards, including the 1989 IEICE Young Engineers Award, 1992 IEEE Andrew R. Chi Best Paper Award, 1997 Okochi Memorial Award, 1998 Japan Microwave Prize, 2000 Ministers Award of the Science and Technology Agency, 2002 and 2011 Asia–Pacific Microwave Conference Prize, 2004 YRP (Yokosuka Research Park) Award, 2006 Asia–Pacific Microwave Photonics Conference Award, 2006 European Microwave Conference Prize, 2007 Achievement Award presented by the IEICE, 2008 Maejima Award, 2011 Recognition from Kinki Bureau of Telecommunications, Ministry of Internal Affairs and Communications, 2011 Commendation for Science and Technology by the Ministry of Education, Culture, Sports, Science and Technology, 2014 IEEE Tatsuo Ito Award, and 2020 Distinguished Achievement and Contributions Award by the IEICE.